PHYSICAL REVIEW B **92**, 214508 (2015)

Superconductivity and crystal structural origins of the metal-insulator transition in $Ba_{6-x}Sr_xNb_{10}O_{30}$ tetragonal tungsten bronzes

Taras Kolodiazhnyi,[1,*] Hiroya Sakurai,[1] Masaaki Isobe,[1] Yoshitaka Matsushita,[1] Scott Forbes,[2] Yurij Mozharivskyj,[2]
Timothy J. S. Munsie,[3] Graeme M. Luke,[3,4] Mary Gurak,[5] and David R. Clarke[5]
[1]*National Institute for Materials Science, 1-1 Namiki, Tsukuba, Ibaraki 305-0044, Japan*
[2]*Department of Chemistry and Chemical Biology, McMaster University, 1280 Main Street West, Hamilton, Ontario L8S 4M1, Canada*
[3]*Department of Physics and Astronomy, McMaster University, 1280 Main Street West, Hamilton, Ontario L8S 4M1, Canada*
[4]*Canadian Institute for Advanced Research, Toronto, Ontario M5G 1Z8, Canada*
[5]*School of Engineering and Applied Sciences, Harvard University, Cambridge, Massachusetts 02138, USA*

(Received 14 July 2015; revised manuscript received 24 September 2015; published 14 December 2015; corrected 13 January 2016)

$Ba_{6-x}Sr_xNb_{10}O_{30}$ solid solution with $0 \leqslant x \leqslant 6$ forms the filled tetragonal tungsten bronze (TTB) structure. The Ba-end member crystallizes in the highest symmetry $P4/mbm$ space group ($a = b = 12.5842(18)$Å and $c = 3.9995(8)$Å) and so do all the compositions with $0 \leqslant x \leqslant 5$. The Sr-end member of the solid solution crystallizes in the tentatively assigned $Amam$ space group ($a^* = 17.506(4)$Å, $b^* = 34.932(7)$Å, and $c^* = 7.7777(2)$Å). The latter space group is related to the parent $P4/mbm$ TTB structure as $a^* \approx \sqrt{2}a$, $b^* \approx 2\sqrt{2}a$, $c^* = 2c$. Low-temperature specific heat measurements indicate that the Ba-rich compositions with $x \leqslant 2$ are conventional BCS superconductors with $T_C \leqslant 1.6$ K and superconducting energy gaps of $\leqslant 0.38$ meV. The values of the T_C in the cation-filled Nb-based TTBs reported here are comparable with those of the unfilled K_xWO_3 and Na_xWO_3 TTBs having large alkali ion deficiency. As the unit cell volume decreases with increasing x, an unexpected metal-insulator transition (MIT) in $Ba_{6-x}Sr_xNb_{10}O_{30}$ occurs at $x \geqslant 3$. We discuss the possible origins of the MIT in terms of the carrier concentration, symmetry break, and Anderson localization.

DOI: 10.1103/PhysRevB.92.214508 PACS number(s): 61.05.cp, 74.25.fc, 74.62.En

I. INTRODUCTION

By their number and chemical diversity compounds with tetragonal tungsten bronze (TTB) structure rival those of perovskites. For example, the metallic TTB $Na_xW_{10}O_{30}$ with $2.8 \leqslant x \leqslant 3.5$ was one of the first discovered metal-oxide superconductors [1] paving the way for a search of superconductivity in other metal oxides. Insulating Nb-based TTB materials have found numerous applications in electronics and optics. For example, ferroelectric (FE) $Ba_{1-x}Sr_xNb_2O_6$ with unfilled TTB structure shows both very large pyroelectric and electro-optic coefficients [2] whereas $Ba_6Ti_2Nb_{10}O_{30}$ and $Pb_6Ti_2Nb_{10}O_{30}$ are extremely efficient second harmonic generators [3].

Compared with the W-based TTBs, studies of the Nb-based TTBs with partially occupied Nb 4*d* electronic band are relatively scarce. Hessen *et al.* have studied $Ba_6Nb_{10}O_{30}$ single crystals obtained from the borate flux and concluded that they crystallize in the TTB aristotype $P4/mbm$ space group [4]. Polycrystalline $Sr_6Nb_{10}O_{30}$ has been also assigned to the same $P4/mbm$ space group [5,6]. The W- and Nb-based TTB compounds with partially occupied *d*-electron orbitals show large crystalline anisotropy of electrical conductivity parallel and perpendicular to the *c* axis [4,7]. In the TTB structure, the columns of the corner-sharing NbO_6 (WO_6) octahedra can be viewed as quasi-one-dimensional (Q1D) chains running along the *c* axis. A combination of the low-dimensionality and soft (ferroelectric-like) lattice dynamics pertinent to the TTB structure may bring an interesting electron correlations, such as unusual superconductivity [8] or Peierls-type charge- and spin-density waves [9].

The TTB is described by a general formula $A1_2A2_4B1_2B2_8C_4O_{30}$ and its schematic structure in the highest symmetry phase (i.e., $P4/mbm$ space group) projected on the *ab* plane is shown in Fig. 1. The unit cell of the $A1_2A2_4B1_2B2_8C_4O_{30}$ consists of a network of ten distorted corner-sharing BO_6 octahedra, which form square (A1-site), pentagonal (A2-site), and triangular (C-site) channels running along the *c* axis. Depending on such factors as the size of the A- and B-site ions, the concentration of the vacant sites and the presence of the lone pair electrons, the TTB structure may exhibit numerous polar and nonpolar distortions accompanied by the symmetry breaking [10–13]. Furthermore, there is a large body of literature that demonstrates one- and two-dimensional incommensurate modulation of both atomic displacements [14–18] and site occupancies [19–21] in the Ba-, Sr-, and Pb-based unfilled TTB compounds, thus raising the maximum crystal symmetry to the (3+2) dimensions.

Recently, Kolodiazhnyi *et al.* demonstrated that in the filled TTB $Ba_{6-x}Sr_xNb_{10}O_{30}$ solid solution there is a close correlation between the amorphouslike low-temperature thermal conductivity and anomalously large atomic displacement parameters of the Ba/Sr atoms [22]. In this contribution we report on more detailed crystal structure analysis of the $Ba_{6-x}Sr_xNb_{10}O_{30}$ and further focus on the electronic, phonon transport, and specific heat properties. In particular, we underline a correlation between the local structural features and metal-insulator phase transition in the title compounds.

II. EXPERIMENTAL METHODS

Single crystals of the Ba- and Sr-end members of the $Ba_{6-x}Sr_xNb_{10}O_{30}$ solid solution were obtained by

---

[*] kolodiazhnyi.taras@nims.go.jp

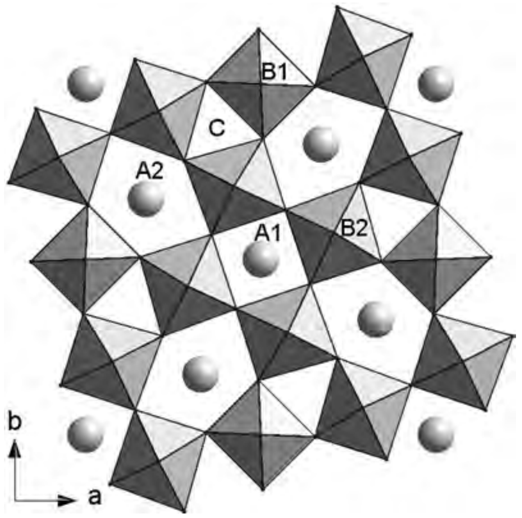

FIG. 1. Schematic drawing of the TTB-type compound $A1_2A2_4C_4B1_2B2_8O_{30}$ viewed along the c axis.

spontaneous crystallization from the melt. A reducing atmosphere was maintained by continuous flow of a H_2/Ar gas mixture. To reduce the melting point 1 wt % of MgO was added to the stoichiometric mixture of $BaCO_3$($SrCO_3$) and Nb_2O_5 [23]. The charge was placed in Mo crucibles, equilibrated for ten hours at 1400 and 1540 °C for $Ba_6Nb_{10}O_{30}$ and $Sr_6Nb_{10}O_{30}$, respectively, cooled down to 1200 °C at 10 °C per hour and furnace cooled to room temperature. The resulting black crystals were removed mechanically from the crucible. In almost all cases the product also contained small amount of nonstoichiometric $Ba_{1-x}NbO_3$ and $Sr_{1-x}NbO_3$ crystals of the dark blue and tyrian purple color, respectively. The volume fraction of these secondary phases could be significantly reduced (but not eliminated completely) by the careful control of the H_2/Ar flow rate.

Preparation details of the polycrystalline $Ba_{6-x}Sr_xNb_{10}O_{30}$ have been reported in Ref. [22]. Ceramics were prepared from 99.99% pure $BaCO_3$ and $SrCO_3$ (Wako Chemicals, Japan) and 99.998% Nb_2O_5 (Cerac, USA). The stoichiometric mixtures were treated at 1000 °C for 10 h in flowing H_2/Ar gas with two intermediate regrindings. Dense ceramic bodies were sintered in flowing H_2/Ar gas at 1360 °C for 10–20 h. The H_2/Ar ratio and flow rate required some fine tuning in order to obtain a single-phase product. Too low H_2/Ar ratio usually resulted in the $Ba_5Nb_4O_{15}$ and $Sr_2Nb_2O_7$ second phases, whereas too high H_2/Ar ratio resulted in the nonstoichiometric $Ba_{1-x}NbO_3$ and $Sr_{1-x}NbO_3$ perovskite second phases. The apparent density of ceramics were better than 95% of theoretical density. The microstructural observations reveal the average grain size of ceramics at around 15 μm.

Single-crystal diffraction data in the temperature range of 100–300 K were collected on a STOE IPDS II diffractometer with Mo K_α radiation. The data were collected until $2\theta = 70^\circ$ in order to obtain precise positional and vibrational parameters for the oxygen atoms. We initially apply a numerical absorption on the crystal shape defined by optical face indexing, but it is later refined against equivalent reflections using the STOE X-SHAPE software. Structural determination and refinement were performed using the SHELXL package [24]. Phase composition of the polycrystalline products was studied by powder x-ray diffraction (Rigaku SmartLab x-ray diffractometer with Cu $K_{\alpha 1}$ x-ray source). Lattice parameters, site occupancies, and isotropic atomic displacement parameters (ADP) were obtained from Rietveld refinement of the x-ray data using JANA2006.

Quantitative elemental composition of the samples was determined by electron probe microanalysis (EPMA) using wavelength-dispersive (WDS) x-ray spectroscopy (model JXA-8500F, JEOL). The EPMA analysis was performed on polished surfaces by averaging the data taken from ten locations of selected area.

Because of the small size of the single crystal, all the physical property measurements were conducted on polycrystalline samples. The ceramics were nearly single phase with the volume of the secondary phases close to the detection limit of the laboratory x-ray diffractometer. A physical property measurements system (PPMS, Quantum Design, USA) equipped with ^{3}He isotope cooling system was used for four-probe resistivity, ρ, Seebeck coefficient, S, and specific heat, C_P, measurements in a temperature range of 0.4–400 K. Magnetic susceptibility, χ, in the same temperature range was studied using magnetic property measurement system (MPMS, Quantum Design, USA) equipped with commercial ^{3}He cryostat from IQUANTUM Corporation. Seebeck coefficient in the 350–1100 K temperature range was measured using ZEM-3 apparatus (ULVAC Technologies, Japan) filled with He gas. High-temperature (350 K $\leqslant T \leqslant$ 1400 K) specific heat, C_P, was measured in flowing argon with Netzsch STA 499 F3 Jupiter thermal analyzer using the sapphire data as a reference. The thermal diffusivity, D, in the $T = 300$–1300 K range was measured in a flowing argon gas with a laser flash method (Netzsch, Micro Flash LFA 457).

III. RESULTS

A. $Ba_6Nb_{10}O_{30}$ and $Sr_6Nb_{10}O_{30}$ single-crystal structure

EPMA analysis of the chemical composition of the selected samples is shown in Table I. All the samples show chemical composition close to the target one. It is noticed that the

TABLE I. EPMA analysis of the chemical composition of selected compounds. All the EPMA data were normalized to six alkali earth atoms.

Target composition	EPMA composition
single-crystal $Ba_6Nb_{10}O_{30}$ + MgO	$Ba_{6.00(4)}Nb_{9.26(8)}Mg_{0.41(3)}O_{28.67(9)}$
single-crystal $Sr_6Nb_{10}O_{30}$ + MgO	$Sr_{6.00(5)}Nb_{10.00(12)}Mg_{0.39(5)}O_{31.94(13)}$
ceramic $Ba_6Nb_{10}O_{30}$	$Ba_{6.00(4)}Nb_{9.57(4)}O_{28.05(6)}$
ceramic $Ba_5SrNb_{10}O_{30}$	$Ba_{4.99(4)}Sr_{1.01(3)}Nb_{9.91(7)}O_{29.16(6)}$
ceramic $Ba_4Sr_2Nb_{10}O_{30}$	$Ba_{4.03(8)}Sr_{1.97(6)}Nb_{10.01(3)}O_{29.26(3)}$
ceramic $Ba_3Sr_3Nb_{10}O_{30}$	$Ba_{3.12(10)}Sr_{2.88(8)}Nb_{10.11(7)}O_{29.79(8)}$
ceramic $Ba_2Sr_4Nb_{10}O_{30}$	$Ba_{2.10(4)}Sr_{3.90(5)}Nb_{10.22(9)}O_{29.69(14)}$
ceramic $BaSr_5Nb_{10}O_{30}$	$Ba_{1.05(3)}Sr_{4.95(5)}Nb_{10.41(7)}O_{31.37(11)}$
ceramic $Sr_6Nb_{10}O_{30}$	$Sr_{6.00(12)}Nb_{10.0(2)}O_{30.6(3)}$

TABLE II. Structure refinement of $Ba_6Nb_{10}O_{30}$ single crystal.

Temperature	293(2) K	100(2) K
Wavelength, Å	0.71073	0.71073
Empirical formula	$Ba_6Nb_{10}O_{30}$	$Ba_6Nb_{10}O_{30}$
Space group	$P4/mbm$	$P4/mbm$
Unit cell dimensions	$a = 12.5842(18)$Å $b = 12.5842(18)$Å $c = 3.9995(8)$Å $\alpha=\beta=\gamma=90^\circ$	$a = 12.5672(18)$Å $b = 12.5672(18)$Å $c = 3.9980(8)$Å $\alpha=\beta=\gamma=90^\circ$
Volume, Å^3	633.37(18)	631.42(18)
Z	2	2
Absorption coefficient, mm^{-1}	13.606	13.648
F(000)	986	986
θ range, °	2.29–34.58	3.24–34.66
Index ranges	$-16 \leqslant h \leqslant 20$ $-19 \leqslant k \leqslant 19$ $-6 \leqslant l \leqslant 6$	$-20 \leqslant h \leqslant 20$ $-20 \leqslant k \leqslant 18$ $-6 \leqslant l \leqslant 6$
Reflections collected	8933	16205
Independent reflections	797 [R(int) = 0.0414]	797 [R(int) = 0.0483]
Completeness to max theta, %	100.0	99.6
Data / restraints / parameters	797 / 0 / 42	797 / 0 / 42
Goodness-of-fit on F^2	1.164	1.201
Final R factors [$I > 2\sigma(I)$]	$R1 = 0.0428$, $wR2 = 0.0900$	$R1 = 0.0492$, $wR2 = 0.1048$
R factors (all data)	$R1 = 0.0498$, $wR2 = 0.0928$	$R1 = 0.0525$, $wR2 = 0.1064$
Extinction coefficient	0.0127(8)	0.0106(8)
Largest peak and hole, e$^-$/Å^3	2.587 and −3.464	3.849 and −3.923

MgO added to reduce the melting temperature of the TTB compounds shows some solubility in the host matrix. Also, it is noticed that the Sr-rich TTBs show slightly higher oxygen content than the Ba-rich TTBs. While the difference in oxygen content may be a genuine feature, it may also be explained by the different tendency toward surface oxidation of the studied compounds.

It was possible to solve the crystal structure of $Ba_6Nb_{10}O_{30}$ crystals at temperatures of 100 K, 150 K, 200 K, 250 K, and room temperature. In agreement with literature data, [4] the $Ba_6Nb_{10}O_{30}$ crystallizes in the $P4/mbm$ space group with $a = b = 12.5842(18)$Å, $c = 3.9995(8)$Å at room temperature, and the R factors are very good (Table II). There is some atomic disorder, specifically for the Ba2 and Nb1 atoms as reflected in the anisotropic displacement parameters listed in Table III of the Supplemental Material [25]. As such, Ba2 and Nb1 had to be refined on different crystallographic sites (Ba2 moved from 4g to 8i, Nb1 moved from 2c to 4f) [26]. The result is an improvement in R factor, better temperature factors, and a reduction of residual electron density. We considered a symmetry break and other space groups, but $P4/mbm$ yields the best solution by far. We collected powder data for this sample as well, but the data does not seem to display peak splitting, indicating that the structure is likely tetragonal. Nb1 has four O4 atoms at 1.958 Å in the ab plane and two O1 at 2.000 Å along the z direction [25]. The large Nb1 vibrations are along the z direction (see Table III of Supplemental Material).

The data for $Sr_6Nb_{10}O_{30}$ crystals were collected at the same temperatures as above. Unfortunately, the $P4/mbm$ symmetry does not seem to describe this structure nearly as well; some of the oxygen atoms have temperature factors about ten times greater than expected. We have considered the possibility of a symmetry reduction, but the results of the x-ray powder data collected are inconclusive. As suggested in the literature, the structure of the parent unfilled $Ba_{1-x}Sr_xNb_2O_6$ TTB compounds can be incredibly complex, with two-dimensional incommensurate modulation [17,19]. From the x-ray single-crystal data collected, we were able to index an orthorhombic A-centered supercell with $a = 17.506(4)$Å, $b = 34.932(7)$Å, $c = 7.7777(2)$Å. This cell may be modeled reasonably well with the $Amam$ space group, although the oxygen atoms must be refined isotropically to obtain reasonable temperature factors. This would suggest possible modulation of the oxygen atoms caused by the buckling of NbO_6 octahedra along the c axis, although we have not been able to model this behavior with complete accuracy. The fractional atomic positions and site symmetry for the $Amam$ structure of $Sr_6Nb_{10}O_{30}$ are given in the Supplemental Material.

B. Crystal structure of $Ba_{6-x}Sr_xNb_{10}O_{30}$ ceramics

Figure 2 shows room temperature powder x-ray patterns of the $Ba_{6-x}Sr_xNb_{10}O_{30}$ ceramics in the 2θ range of 33.6–41.5 degrees, whereas Fig. 3 shows x dependence of the unit cell and isotropic atomic displacement parameters of the $0 \leqslant x \leqslant 5$ ceramics. Preliminary results of the crystal structure analysis of the $Ba_{6-x}Sr_xNb_{10}O_{30}$ ceramics have been reported by Kolodiazhnyi *et al.* [22]. In Ref. [22] all compositions of the $Ba_{6-x}Sr_xNb_{10}O_{30}$ solid solution (i.e., $0 \leqslant x \leqslant 6$) were refined within the $P4/mbm$ space group. Indeed the $Ba_{6-x}Sr_xNb_{10}O_{30}$ with $0 \leqslant x \leqslant 5$ are well refined within the $P4/mbm$ space group in agreement with the $Ba_6Nb_{10}O_{30}$ single crystal data. After more careful analysis we note,

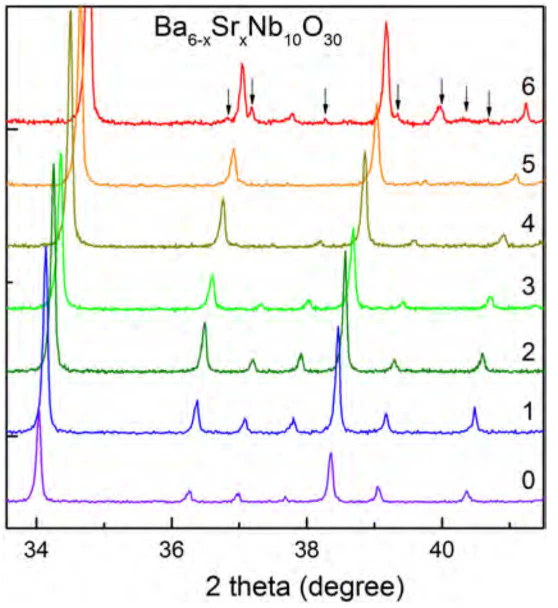

FIG. 2. (Color online) Room temperature powder x-ray diffraction patterns of $Ba_{6-x}Sr_xNb_{10}O_{30}$ in the 2θ range of 33.6–41.5 degrees. The numbers above each pattern indicate the x value. The vertical arrows above the $x = 6$ pattern indicate the reflections that cannot be indexed in the $P4/mbm$ space group.

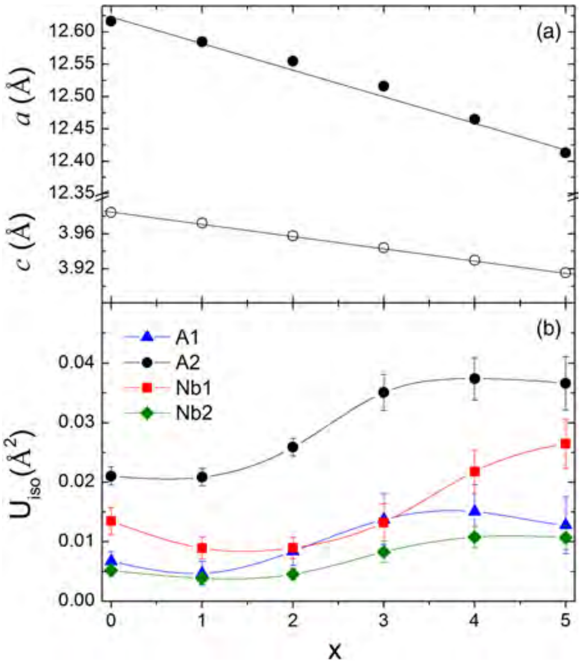

FIG. 3. (Color online) (a) Evolution of the lattice constants a and c as a function of Sr content, x, in $Ba_{6-x}Sr_xNb_{10}O_{30}$. A positive deviation from the Vegard's law for a is probably originating from the selective preferential occupation of the A1 and A2 sites. (b) Isotropic displacement parameters, U_{iso}, for A1, A2, Nb1, and Nb2 lattice sites as a function of x. Vertical bars represent one standard deviation. The lines are the guides for the eye.

however, that the quality of the $P4/mbm$ fit is less satisfactory for $x = 6$. Moreover, some of the weak reflections that appear in the Sr end member in Fig. 2 cannot be fitted with the $P4/mbm$ space group. Obviously, the $Sr_6Nb_{10}O_{30}$ ceramics has a lower symmetry than the $Ba_6Nb_{10}O_{30}$ aristotype. After exhaustive search, we have found that the orthorhombic *Amam* space group [$a = 17.4785(3)$Å, $b = 34.9424(6)$Å, $c = 7.79737(4)$Å] gives the best fit to the powder diffraction pattern. It is also in good agreement with the $Sr_6Nb_{10}O_{30}$ single-crystal solution. [25]

Figure 4 shows the *Amam* [Fig. 4(a)] and $P4/mbm$ [Fig. 4(b)] fits to the $Sr_6Nb_{10}O_{30}$ powder diffraction pattern in the selected 2θ range. It is clear that the orthorhombic structure gives a much better solution than the tetragonal one. Also, the latter one cannot describe numerous weak reflections in the diffraction data as demonstrated in Fig. 4(b). The lowering of the symmetry in the TTB structure may be intuitively understood as a result of the decrease in the ionic size of the A-site ion. For example, substitution of Sr^{2+} and Eu^{2+} for larger size Ba^{2+} often results in octahedral buckling along the c axis and concomitant doubling of the unit cell [27,28]. Nevertheless, many oxygen atomic displacement parameters of the *Amam* structure were not positive definite. As such, the *Amam* assignment must be treated with caution because it may not be a true crystal structure solution for Sr-rich $Ba_{6-x}Sr_xNb_{10}O_{30}$. The origin of the nonpositive definite ADPs of the oxygen atoms in the $Sr_6Nb_{10}O_{30}$ *Amam* structure may lie in the possible existence of incommensurate modulations, which, unfortunately, are beyond our crystal analysis skills. It is known that the closely related $Ba_{1-x}Sr_xNb_2O_6$ and $Ba_{1-x}Ca_xNb_2O_6$ with unfilled TTB structure crystallize in incommensurately modulated noncentrosymmetric tetragonal $X4bm(pp1/2,\ p\text{–}p1/2)$, $X4bm(AA0,\ \text{–}AA0)$, or orthorhom-

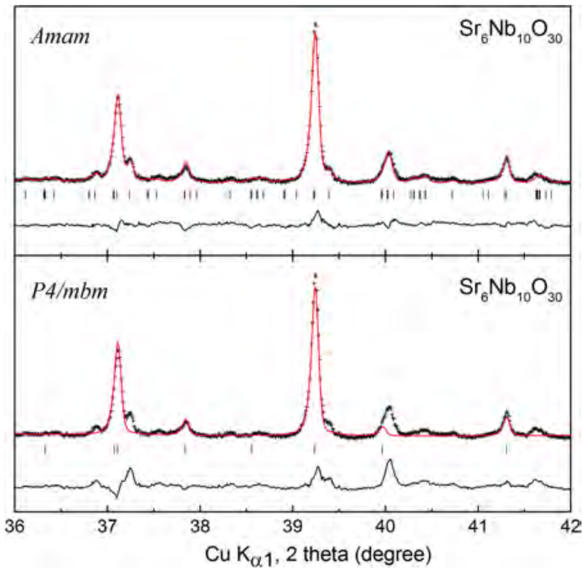

FIG. 4. (Color online) Room temperature Rietveld refinement of $Sr_6Nb_{10}O_{30}$ with (a) *Amam* space group [$a = 17.4785(3)$Å, $b = 34.9424(6)$Å, $c = 7.79737(4)$Å] GOF = 3.00%, $R_p = 5.19\%$, $R_{wp} = 7.27\%$; (b) $P4/mbm$ [$a = b = 12.35425(7)$Å, $c = 3.89797(3)$Å] GOF = 3.64%, $R_p = 6.30\%$, $R_{wp} = 8.91\%$. The cross marks are data points, red line is the fit, vertical bars are expected Bragg reflections. Black lines at the bottom are the difference between the experimental data and the fit.

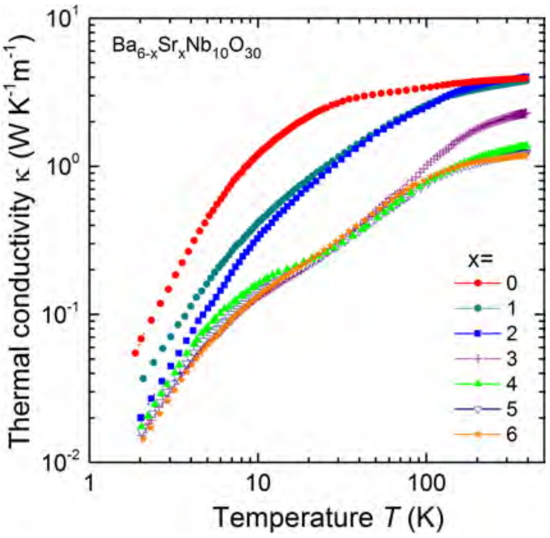

FIG. 5. (Color online) Concentration dependence of the thermal conductivity of polycrystalline $Ba_{6-x}Sr_xNb_{10}O_{30}$.

bic $X2mm(00\gamma)000$ superspace groups [17,18]. Noteworthy in $Ba_{1-x}Sr_xNb_2O_6$, the amplitudes of the positional modulation increase as a function of the strontium substitution x [20]. According to Schefer *et al.* and Graetsch *et al.*, the origin of the displacive modulation of the O atoms lie in a modulation of the occupancy of the A2 site with fifteenfold oxygen coordination [20,21]. It is not clear, though, if the above modulation scenario is applicable to the title TTB compounds. None of them contains intentional vacancies on the A2 sites. Furthermore, the Sr-end member has no atomic-type modulation because all the A2 sites are filled with the same Sr atoms. Further electron diffraction studies of the title compounds are underway to clarify the crystal symmetry.

C. Thermal conductivity

Preliminary results on the thermal conductivity, κ, of the $Ba_{6-x}Sr_xNb_{10}O_{30}$ were reported in Ref. [22]. For a typical crystalline material, at a very low temperatures, κ is determined by the acoustic phonon scattering on the external boundary of the sample, which takes the form of $\kappa \propto T^3$ and is followed by a κ maximum at $T \approx 20$–30 K depending on the concentration of the defects [29]. At higher temperatures thermal conductivity is determined by the phonon scattering with $\kappa \propto T^{-1}$. None of the title compounds show κ dependence typical of a good crystal (see Fig. 5). Most interesting, a suppression in the $\kappa(T)$ dependence reminiscent of that found in amorphouslike materials develops at $x \geqslant 3$. In Ref. [22] this plateaulike κ anomaly was assigned to the anomalous atomic displacement parameters of the A1 cations [30]. While it is not clear whether the large atomic displacement parameters of the A1 and B1 cations have a static or dynamic origin they seem also to have a very strong influence on the electron transport discussed below.

D. dc resistivity

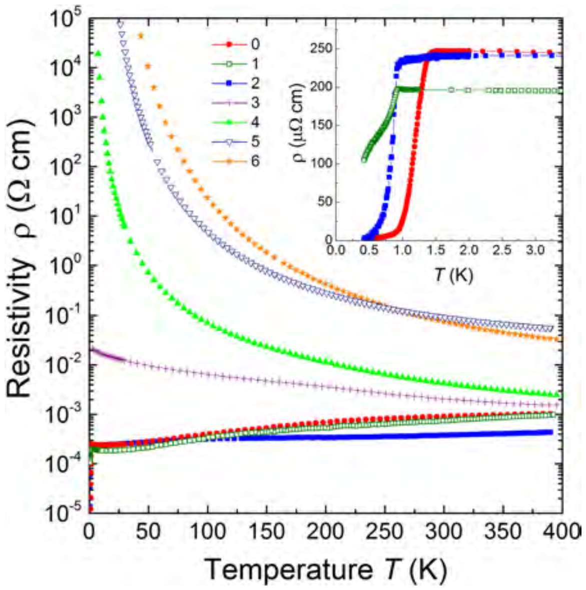

FIG. 6. (Color online) Temperature dependence of the dc resistivity of $Ba_{6-x}Sr_xNb_{10}O_{30}$ for different Sr substitution x. The inset shows the low-T resistivity for $Ba_{6-x}Sr_xNb_{10}O_{30}$ with $x = 0$, 1, 2.

The isotropic dc resistivity, ρ, of the $Ba_{6-x}Sr_xNb_{10}O_{30}$ ceramics is shown in Fig. 6. In contrast to Refs. [4,6] our $Ba_6Nb_{10}O_{30}$ sample is metallic as well as the other Ba-rich compounds with $x \leqslant 2$. Metal-to-insulator transition is observed with increasing Sr content x. Compounds with $x \geqslant 4$ show divergent resistivity at low temperatures pointing to their insulating ground state. Attempts to determine the energy gap for thermal activation of the charge carriers of the $x \geqslant 4$ compounds were not successful because of the non-Arrhenius ρ vs. T dependence. Instead, we found that variable range hopping (VRH) describes quite well the temperature dependence of the resistivity. The VRH resistivity in the d-dimensional systems is given by [31]:

$$\rho \propto \exp\left\{\frac{T_0}{T}\right\}^{\frac{1}{d+1}}, \tag{1}$$

where d is the dimensionality of the system and T_0 is the constant. Figure 7 shows a fit of the VRH model to the experimental resistivity data for samples $x = 4$, 5, and 6. The resistivity of samples $x = 5$ and 6 follows well the VRH model for a one-dimensional system up to $T = 273$ and 200 K, respectively [Fig. 7(a)]. Sample $x = 4$, on the other hand, follows the VRH model for a two-dimensional system up to $T = 240$ K [Fig. 7(b)].

By analogy with Na- and K-doped WO_3 bronzes, we assume that each Ba^{2+}/Sr^{2+} ion that fills up the A-site cation vacancy brings two electrons to the conduction band of the TTB. Therefore, a filled $Ba_{6-x}Sr_xNb_{10}O_{30}$ structure will have two itinerant electrons per formula unit, which is equivalent to the charge carrier concentration of $n \approx 1.58 \times 10^{21}$ cm^{-3}. Based on this assumption, the room-temperature isotropic electron mobility, $\mu = (e \times n \times \rho)^{-1}$, where e is the electron charge, range from 3.9–11 cm^{2}V^{-1}s^{-1} for metallic samples (i.e., $x \leqslant 2$). These mobilities are comparable with those of metallic Na-doped WO_3 bronzes [7]. At the same time, the

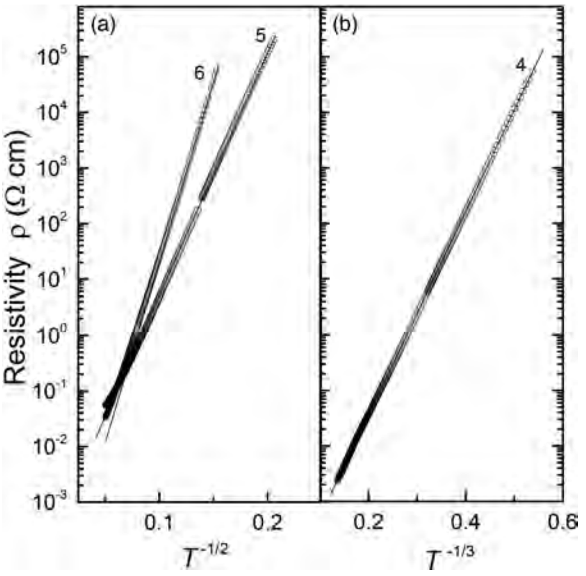

FIG. 7. Low-dimensional variable range hopping fit to the dc resistivity of (a) samples $x = 5$, 6 and (b) sample $x = 4$. The lines are the fit to one-dimensional VRH with $\ln\rho \propto T^{-1/2}$ (a) and two-dimensional VRH with $\ln\rho \propto T^{-1/3}$ (b).

$\mu = 258\ \mathrm{cm^2\ V^{-1}s^{-1}}$ parallel to the c axis in $Ba_6Nb_{10}O_{30}$ single crystal reported by Hessen *et al.* [4], looks highly unusual and may require additional confirmation upon availability of the high-quality single crystal.

In addition to the unusual metal-to-insulator phase transition in $Ba_{6-x}Sr_xNb_{10}O_{30}$ that takes place upon contraction of the unit cell volume, there is another important low-T feature in Fig. 6. Namely, Ba-rich compounds with $x \leqslant 2$ demonstrate a superconducting transition at $T \leqslant 1.6$ K as shown more clearly in the inset of Fig. 6. Sample $x = 1$ shows an incomplete superconducting phase transition with an onset temperature of ≈ 0.94 K. The possible reason for the nonzero residual resistivity of the $x = 1$ compound may be due to the blocking secondary phase at the grain boundary regions. Although the superconductivity in the W-based TTB has been known for five decades [1], none has been reported for Nb-based TTB so far. The temperature of the onset of the superconductivity and the volume fraction of the superconducting phase were estimated from the magnetic and specific heat measurements reported below.

E. Magnetic properties

Superconductivity in Ba-rich $Ba_{6-x}Sr_xNb_{10}O_{30}$ is confirmed by magnetic measurements. Figure 8 shows an onset of magnetic anomaly associated with the Meissner effect for selected $Ba_{6-x}Sr_xNb_{10}O_{30}$ samples, $x = 0$, 1, 2. In the case of sample $x = 1$ we noticed the paramagnetic Meissner effect, which is sometimes seen in polycrystalline anisotropic superconductors, which can give a nonreliable measure of the superconducting volume fraction [32]. The temperature of the onset of the magnetic flux shielding effect determined by the magnetic measurements is in agreement with the resistivity data (inset of Fig. 6). The volume fraction of the shielding phase was estimated from the volume magnetic susceptibility (Fig. 9) of the samples cooled down in zero magnetic field. The shielding volume fraction of the $x = 0$ and $x = 2$ samples equal approximately 15 and 30 %, respectively. While it seems to be too low, it is known, however, that the volume fraction of the superconducting phase in the powder sample of the highly anisotropic materials determined by magnetic measurements is significantly underestimated. For example, the magnetic susceptibility of layered $Na_xCoO_2 \cdot yH_2O$ polycrystal in its superconducting phase is 6.5% of the theoretical value for a perfect diamagnet [33]. The FC susceptibility in Fig. 9 is much smaller than expected for a full flux expulsion, presumably due to flux pinning, which would be strong in an anisotropic, polycrystalline superconductor.

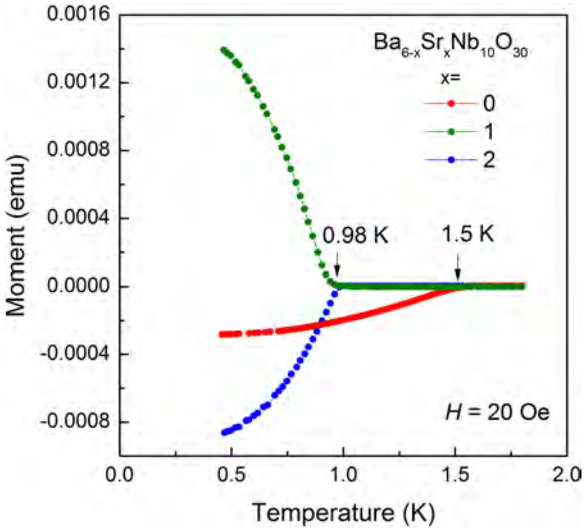

FIG. 8. (Color online) Temperature dependence of magnetic moment for zero-field cooled $Ba_{6-x}Sr_xNb_{10}O_{30}$ samples $x = 0$, 1, and 2.

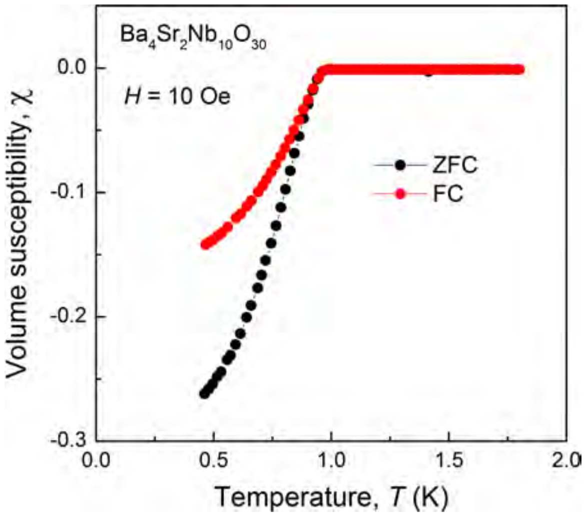

FIG. 9. (Color online) Temperature dependence of the volume magnetic susceptibility for $Ba_4Sr_2Nb_{10}O_{30}$. ZFC and FC indicate zero-field-cooled and field-cooled data, respectively.

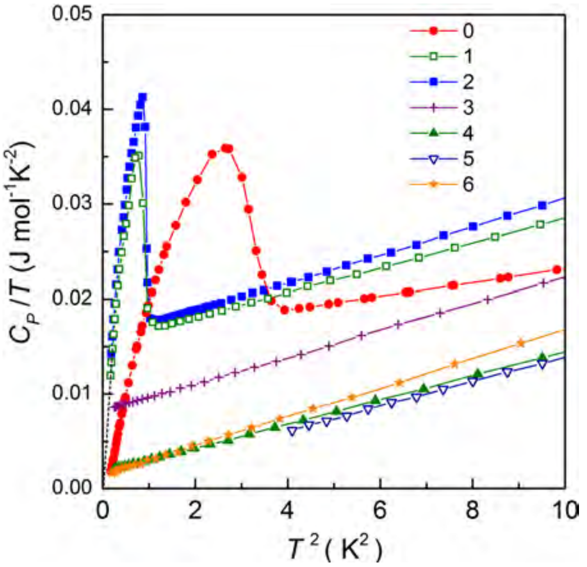

FIG. 10. (Color online) C_P/T vs. T^2 dependence for $Ba_{6-x}Sr_xNb_{10}O_{30}$. The x value is indicated in the legend. The lines are the guides for the eye.

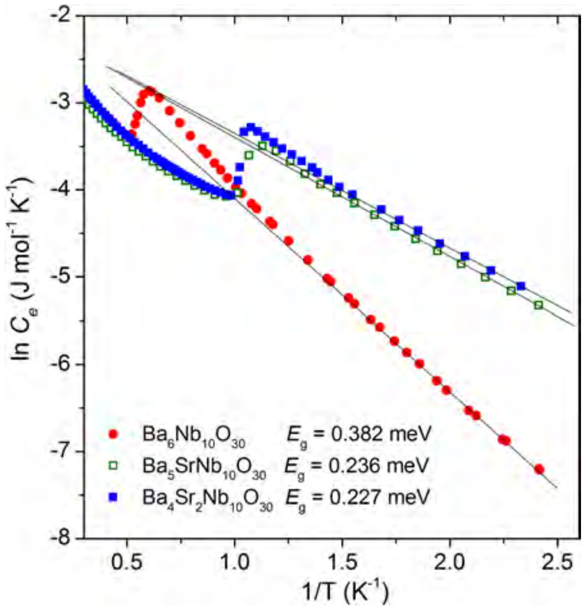

FIG. 11. (Color online) Arrhenius dependence of C_e of $Ba_{6-x}Sr_xNb_{10}O_{30}$ for samples with $x = 0$, 1, and 2.

F. Specific heat and thermal diffusivity

To obtain a better idea about the nature of the superconducting phase transition and the volume of the superconducting phase, we performed low-temperature measurements of specific heat, C_P, of the $Ba_{6-x}Sr_xNb_{10}O_{30}$ ceramics. The λ-type anomaly in C_P data was detected for samples with $x \leqslant 2$. Figure 10 shows the C_P/T vs. T^2 dependence. From these data it can be seen that for $x \leqslant 2$ the residual Sommerfeld coefficient, $\gamma_r = C_P/T$, approaches zero at $T \to 0$. Therefore, the volume of the nonsuperconducting phase in the $x \leqslant 2$ samples, $V = \gamma_r/\gamma_n$, where γ_n is the Sommerfeld coefficient of the normal state, is close to zero. The temperatures of the C_P maxima in the superconducting samples are in agreement with the resistivity and magnetic data. To estimate the superconducting energy gap, $E_g = 2\Delta$, we first subtracted the lattice contribution, $C_{\text{lat}} = \beta T^3$, to the specific heat (Fig. 3 in Supplemental Material) and then plotted the electronic part of specific heat, C_e, vs. T^{-1} in Fig. 11. Assuming that the title compounds are conventional BCS superconductors, the energy gap in the superconducting density of states was estimated from the Arrhenius dependence of electronic contribution of the specific heat at $T \ll T_C$:

$$C_e \propto \exp\left\{-\frac{\Delta}{k_B T}\right\}, \tag{2}$$

where k_B is the Boltzmann constant. The linear fit to Eq. (2) is shown in Fig. 11. Several thermodynamic parameters including T_C, γ_n, E_g, specific heat jump: $\frac{\Delta C_e}{\gamma_n T_C}$, the gap over T_C ratio: $\frac{E_g}{k_B T_C}$ and the β coefficient of the lattice specific heat are summarized in Table III.

In view of a good exponential fit of the low-temperature specific heat data to Eq. (2) at $T \ll T_C$, we conclude that the title compounds are conventional s-wave superconductors without any evidence of the nodal lines or nodal points [34]. The BCS theory predicts the ratio of the specific heat jump at T_C, $\frac{\Delta C_e}{\gamma_n T_C} = 1.43$. The studied ceramics show $\frac{\Delta C_e}{\gamma_n T_C}$ ranging from 1.31–1.60. These values are slightly higher than that reported for K_xWO_3 TTB weakly electron-phonon-coupled superconductors with comparable T_C [35].

The metal-to-insulator transition at $x > 3$ is reflected in the drop of the γ_n as a function of Sr content shown in Fig. 12. It is noteworthy, however, that the Sommerfeld coefficient does not vanish for insulating samples with $x \geqslant 4$. This is another evidence that some degree of lattice disorder exists in the title compounds, which gives a small linear contribution to the low-T specific heat even in the absence of the Fermi surface. Indeed, a small, nonzero γ_n appears to be a signature of the TTB- and perovskite-based relaxor ferroelectrics that also show amorphouslike low-T thermal conductivity [36,37]. It is attributed to the existence of the two-level density of states that enhances the low-T C_P above the C_{lat} contribution [38].

Figure 13 shows the specific heat of several $Ba_{6-x}Sr_xNb_{10}O_{30}$ samples measured in a wide temperature range up to 1500 K. The samples with $x \leqslant 4$ show no detectable anomalies in the high-T specific heat data. We bring attention to the two high-temperature phase transitions

TABLE III. Physical properties of superconducting $Ba_{6-x}Sr_xNb_{10}O_{30}$ ceramics.

x, compound	0	1	2
T_C, K	1.65	0.96	0.98
γ_n, mJ mol^{-1}K^{-2}	17.09	15.75	16.82
E_g, meV	0.382	0.236	0.227
$\frac{\Delta C_e}{\gamma_n T_C}$	1.31	1.56	1.60
$\frac{E_g}{k_B T_C}$	2.69	2.85	2.69
β, mJ mol^{-1}K^{-4}	0.37	1.15	1.04

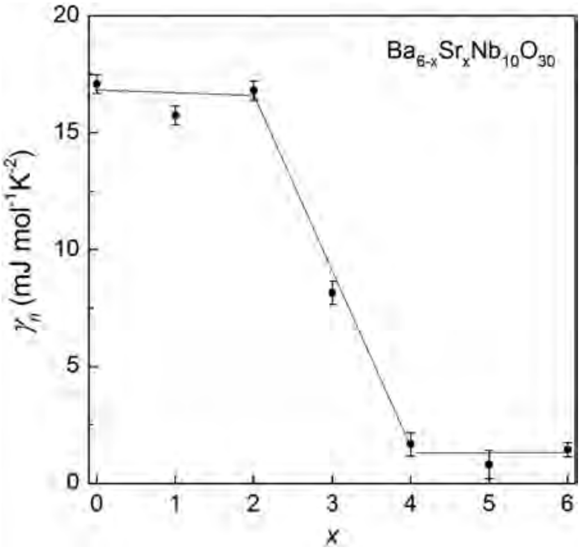

FIG. 12. Sommerfeld coefficient of the normal state of $Ba_{6-x}Sr_xNb_{10}O_{30}$ as a function of Sr content x. The lines are the guides for the eye.

in the $Sr_6Nb_{10}O_{30}$. The first phase transition with a very broad maximum at $T \approx 720$ K is somewhat similar to that observed in the noncentrosymmetric $Ba_{1-x}Sr_xNb_2O_6$ unfilled TTBs [39]. At $T \approx 1072$ K another sharp phase transition with a first-order signature is detected (Fig. 13). The later phase transition is very similar to that found by one of us in the $SrTa_2O_6$ and $EuTa_2O_6$ TTBs (not shown here) and is most likely attributed to the doubling of the TTB unit cell along the c axis. A very broad and weak anomaly in the specific heat of the $BaSr_5Nb_{10}O_{30}$ sample is indicated by a vertical arrow at $T \approx 702$ K in Fig. 13. This C_P feature is quite weak and is close to the detection limit of our apparatus. It may be associated with a very small structural change in the $BaSr_5Nb_{10}O_{30}$ compound. If true, this structural transition must be very weak because we could not detect any symmetry reduction from the $P4/mbm$ space group in the room temperature x-ray powder diffraction data of $BaSr_5Nb_{10}O_{30}$.

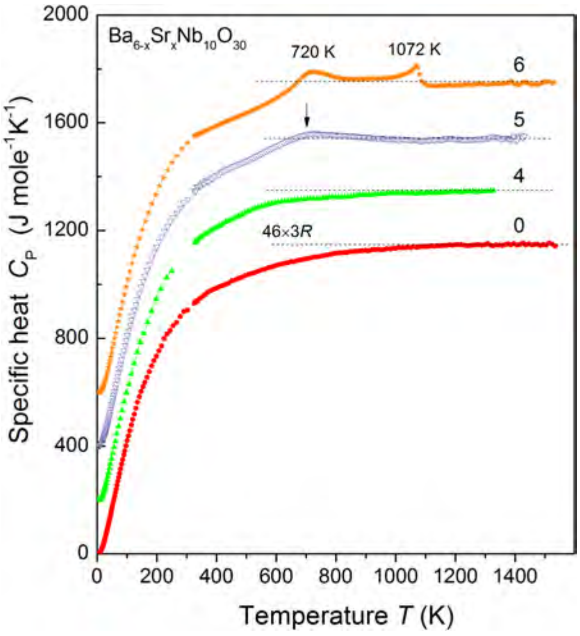

FIG. 13. (Color online) Specific heat of the selected $Ba_{6-x}Sr_xNb_{10}O_{30}$ samples in a wide temperature range. The numbers correspond to the value of x. The data are offset by 200 J mol^{-1}K^{-1} for clarity of presentation. The dashed lines correspond to the high-temperature specific heat limit of 46 × 3R. A vertical arrow indicates a broad anomaly in specific heat of the $BaSr_5Nb_{10}O_{30}$.

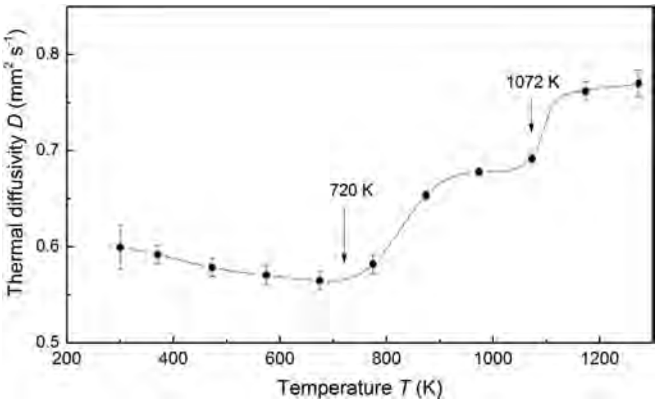

FIG. 14. High-temperature thermal diffusivity of $Sr_6Nb_{10}O_{30}$. The arrows indicate the temperatures of the phase transitions as determined from the specific heat data shown in Fig. 13. The line is a guide for the eye.

Figure 14 shows high-temperature thermal diffusivity of $Sr_6Nb_{10}O_{30}$. Thermal diffusivity is highly sensitive to the structural phase transitions in ferroelectric perovskites and TTB compounds [39,40]. In the absence of the structural phase transitions, the thermal diffusivity usually decreases gradually with temperature due to the decrease in the phonon scattering length. The two steplike features marked by the vertical arrows in the thermal diffusivity of the $Sr_6Nb_{10}O_{30}$ (Fig. 14) are closely correlated with the phase transitions at the similar temperatures as detected by the specific heat measurements (see Fig. 13). A pronounced increase in D at these temperatures is associated with an increase in the phonon scattering length as a result of the lifting in the crystal symmetry [39].

G. Seebeck coefficient

Temperature evolution of the Seebeck coefficient, S, of the $Ba_{6-x}Sr_xNb_{10}O_{30}$ is shown in Fig. 15. As expected, the $Ba_{6-x}Sr_xNb_{10}O_{30}$ with $x \leqslant 3$ show metal-like behavior with S increasing gradually with temperature. The samples with insulating ground state (i.e., $x \geqslant 4$) show much higher S with a somewhat more complex temperature dependence. To better understand this behavior we have expanded the thermopower measurement range for the end members to $T = 1100$ K. Somewhat poor match between the low- and high-T data in the 350–400 K interval is explained by the use of two different experimental setups below and above 400 K. The Seebeck coefficient of the $Ba_6Nb_{10}O_{30}$ end member continues to gradually increase, as expected for metals. The S of $Sr_6Nb_{10}O_{30}$, on the other hand, shows a pronounced anomaly with a strong dip at $T \approx 800$ K followed by a steady increase at higher temperatures characteristic of a metal (Fig. 15). It is

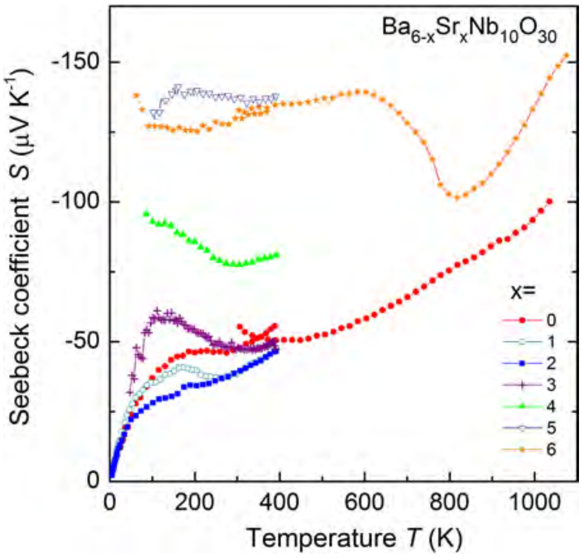

FIG. 15. (Color online) Temperature dependence of Seebeck coefficient of $Ba_{6-x}Sr_xNb_{10}O_{30}$.

noteworthy that the steepest drop in the Seebeck coefficient in the $Sr_6Nb_{10}O_{30}$ sample at $T \approx 750$ K correlates reasonably well with the broad phase transition at $T \approx 720$ K as detected by specific heat measurements. We speculate, therefore, that the transition from the insulating to metallic-type behavior in $Sr_6Nb_{10}O_{30}$ may be associated with the structural phase transition at 720 K.

Assuming spherical shape of the Fermi surface, the Seebeck coefficient in the high-temperature phonon-scattering region is given by:

$$S = \frac{\pi^2 k_B^2 T}{E_F}, \tag{3}$$

where E_F is the Fermi energy. From Eq. (3) we estimate the Fermi energy of the $Sr_6Nb_{10}O_{30}$ and $Ba_6Nb_{10}O_{30}$ in the metallic phase at 527 and 767 meV, respectively. Assuming the similar electron count, the difference in the E_F may come from the different effective electron mass and the density of states at the Fermi level. Because of highly anisotropic crystal structure of the TTB, it is unlikely that the Fermi surface is spherical and the above estimate of the Fermi energy has to be taken with caution.

IV. DISCUSSION

Following the Goodenough model [41], and ignoring the effect of spin-orbit coupling, we expect that the lowest part of the conduction band in the $Ba_{6-x}Sr_xNb_{10}O_{30}$ TTBs is formed by the antibonding σ^* and π^* bands comprised by the $4d$ Nb and $2p$ O orbitals (i.e., $pd\sigma$ and $pd\pi$ overlaps). The octahedral ligand field formed by the nearest-neighbor oxygens will result in the high-energy doubly degenerate e_g and low-energy triply degenerate t_{2g} bands. Furthermore, in the $Ba_6Nb_{10}O_{30}$ the oxygen octahedron around the Nb1 atom is tetragonally distorted: with ×4 Nb1-O4 bond length of 1.959(6) Å in the ab plane and ×2 Nb1-O1 bond length of 1.9998(4) Å along the c axis [25]. This will further split the π^* band into the lower-energy doubly degenerate $\pi^*_{xz,yz}$ and a higher-energy nondegenerate π^*_{xy}. The situation is more complex with the Nb2 atom because of highly distorted ligand environment. The Nb2 atom in $Ba_6Nb_{10}O_{30}$ has four different bond length with oxygens in the ab plane as well as reduced [i.e., O3-Nb2-O3 = 175.5(4)°] bond angle along the z direction [25]. As such, it is difficult to predict the correct symmetry of the lowest-energy conduction electron band in this case. Nevertheless, we can make a very crude estimate of the d-electron spacial distribution based on the bond valence sum (BVS) calculations [42]. According to the Nb-O bond distances for the $Ba_6Nb_{10}O_{30}$ single crystal [25], the BVS calculation predicts the oxidation states of the Nb1 and Nb2 ions to be approximately 5.095 and 4.803, respectively. This may indicate the tendency for electron localization on the Nb2 ions, which has lower local symmetry than the Nb1 ion (see Fig. 1). The first-principles electron band calculations of the Nb-based TTBs would be very helpful to resolve these issues.

In view of the above, how can we explain the MIT in the $Ba_{6-x}Sr_xNb_{10}O_{30}$ series? First, we rule out strong electron correlation due to Hubbard mechanism because the Nb $4d^\delta$ band is only partially filled with electrons (i.e., $\delta \approx 0.2$) and there is no reason for a large Coulomb repulsion (Mott-Hubbard gap) for electron transfer [43]. The absence of the Mott-Hubbard gap is also supported by the metallic ground state of the $SrNbO_3$ with much higher electron occupancy of the Nb $4d^\delta$ band (i.e., $\delta \approx 1$) and a similar Nb-O-Nb bond distance [44]. The remaining three mechanisms of the MIT in $Ba_{6-x}Sr_xNb_{10}O_{30}$ may include (i) Mott-type MIT driven by a symmetry break, (ii) Anderson-type localization, and (iii) critical electron concentration. We discuss them below in detail.

(i) The $pd\sigma$ and $pd\pi$ overlap energy integrals are sensitive to both the bond length and the bond angle [45]. In many cases the bond angle plays a more important role than the bond length in the d-electron systems. For example, a transition from the metallic to nonmetallic conductivity occurs in the $Sr_{1-x}Ca_xNbO_3$ with increasing x during the orthorhombic distortion of the perovskite unit cell: $a \approx c \approx \sqrt{2}\times a_{\text{per}}$, $b \approx 2\times a_{\text{per}}$, notwithstanding an overall contraction of the unit cell volume [46]. In the metallic $Ba_6Nb_{10}O_{30}$ with a $P4/mbm$ symmetry, the Nb1-O1-Nb1 and Nb2-O3-Nb2 bond angles are 180° and 175.5°, respectively. In the nonmetallic $Sr_6Nb_{10}O_{30}$ with the $Amam$ symmetry, all the Nb-O-Nb bond angles along the c axis are notably smaller than 180° [25]. Therefore, a decrease in the Nb-O-Nb bond angle from the optimal value of 180° induced by the $P4/mbm \rightarrow Amam$ phase transition will decrease the overlap energy integral and may be the reason behind the MIT in $Ba_{6-x}Sr_xNb_{10}O_{30}$. Within this mechanism, the MIT in the $Ba_{6-x}Sr_xNb_{10}O_{30}$ can be classified as Mott-type transition, which is driven by the angle-dependent overlap between the highly anisotropic Nb $4d$ and O $2p$ orbitals [43]. The obvious problem with this model is that it cannot explain the insulating ground state in the high-symmetry Sr-rich TTB members. Only the $Sr_6Nb_{10}O_{30}$ end member of the $Ba_{6-x}Sr_xNb_{10}O_{30}$ series shows the reduced crystal symmetry ($Amam$ phase), other members of the series, including those with insulating ground state, remain in the $P4/mbm$ space group according to our laboratory x-ray diffraction analysis.

(ii) Anderson-type electron localization due to random electric field is more likely mechanism of MIT in $Ba_{6-x}Sr_xNb_{10}O_{30}$. As discussed in Ref. [22] the TTB structure develops an intrinsic disorder when small Sr ion substitutes larger Ba ion on the A2 crystallographic site (Fig. 1). This intrinsic disorder is evidenced by the large atomic displacement parameters of the Sr and Nb ions [25]. It is also manifested in the amorphouslike thermal conductivity that develops in the $Ba_{6-x}Sr_xNb_{10}O_{30}$ for $x \geqslant 3$ (Fig. 5). In this case, the random electric field potential, V_0, may be comparable to the width of the $\pi^*_{xz,yz}$ conduction band, B, leading to the localization of the itinerant electrons at some critical value of V_0/B [47]. It is noteworthy that the onset of both the low-T amorphouslike thermal conductivity and the MIT occur at the similar value of Sr substitution $x \approx 3$ (see Figs. 5 and 6).

(iii) We note that our metallic resistivity data are at variance with the semiconducting behavior of $Ba_6Nb_{10}O_{30}$ reported in literature [4,6]. This calls for a check whether the Mott criterion for MIT in the $Ba_{6-x}Sr_xNb_{10}O_{30}$ series is satisfied. According to Ref. [48] an insulator to metal transition will occur when electron concentration exceeds the critical value, n_c, given by:

$$n_c = \left[\frac{\xi m^* e^2}{\varepsilon \hbar^2}\right]^3, \tag{4}$$

where $m^* = m_0$ is effective electron mass (here assumed to be equal to the bare electron mass, m_0), $\varepsilon = 174$ is the static low-temperature dielectric constant of $Sr_6Nb_{10}O_{30}$, $\hbar$ is the Planck constant and $\xi \approx 0.25$–0.4. Considering the Q1D nature of the $Ba_{6-x}Sr_xNb_{10}O_{30}$ and electron localization on the Nb d orbitals, it is reasonable to use an upper limit of ξ (i.e., $\xi = 0.4$) which gives $n_c \approx 1.1 \times 10^{17}$ cm^{-3}. Yet, this is four orders of magnitude smaller than electron density $n \approx 1.58 \times 10^{21}$ cm^{-3} in stoichiometric $Ba_{6-x}Sr_xNb_{10}O_{30}$. Therefore, according to Mott criterion, all the $Ba_{6-x}Sr_xNb_{10}O_{30}$ series must be metallic, which is not supported by our experimental data. This provides further evidence in favor of the Anderson-type electron localization that drives MIT in the $Ba_{6-x}Sr_xNb_{10}O_{30}$ series.

V. CONCLUSIONS

A series of the filled TTB $Ba_{6-x}Sr_xNb_{10}O_{30}$ compounds crystallize in the high-symmetry tetragonal $P4/mbm$ structure for $0 \leqslant x \leqslant 5$. As the volume of the unit cell decreases with increasing x, an unusual MIT occurs at $x \approx 3$ in an absence of the long-range symmetry break. The Sr-end member of the $Ba_{6-x}Sr_xNb_{10}O_{30}$ series shows orthorhombic distortion tentatively assigned to the *Amam* space group. We discuss three possible scenarios that may drive the metal to insulator transition in the $Ba_{6-x}Sr_xNb_{10}O_{30}$ solid solution. We favor the Anderson-type electron localization model as it explains the MIT not only in the low-symmetry $Sr_6Nb_{10}O_{30}$ end member but also in a high-symmetry $Ba_{6-x}Sr_xNb_{10}O_{30}$ compounds. This model is also supported by the low-temperature amorphous-type thermal conductivity observed in all the insulating $Ba_{6-x}Sr_xNb_{10}O_{30}$ compounds. On the metallic side of the MIT, compositions with $x \leqslant 2$ show superconducting properties with $T_C \leqslant 1.6$ K. In contrast to the well-studied unfilled W-based TTBs, this is an account of superconductivity in the filled Nb-based TTBs. Proximity to the structural phase boundary gives the highest T_C in W-based TTBs [8,35]. It remains to be explored whether this model also works for Nb-based TTBs.

ACKNOWLEDGMENTS

The authors thank Dr. M. Onoda and Dr. Y. Michiue for valuable discussions of the incommensurate lattice modulation, K. Suzuta and Dr. H. Tanaka for high-temperature specific heat measurements, and K. Kosuda for electron probe microanalysis. This work was supported by Grant-in-Aid for Scientific Research C 26400323 from JSPS.

---

[1] Ch. J. Raub, A. R. Sweedler, M. A. Jensen, S. Broadston, and B. T. Matthias, Phys. Rev. Lett. **13**, 746 (1964).
[2] A. S. Bhalla, R. Guo, L. E. Cross, G. Burns, F. H. Dacol, and R. R. Neurgaonkar, Phys. Rev. B **36**, 2030 (1987).
[3] E. O. Chi, A. Gandini, K. M. Ok, L. Zhang, and P. S. Halasyamani, Chem. Mater. **16**, 3616 (2004).
[4] B. Hessen, S. A. Sunshine, A. T. Siegrist, A. T. Fiory, and J. V. Wazczak, Chem. Mater. **3**, 528 (1991).
[5] B. Hessen, S. A. Sunshine, T. Siegrist, and R. Jimenez, Mater. Res. Bull. **26**, 85 (1991).
[6] Y. K. Hwang and Y.-U. Kwon, Mater. Res. Bull. **32**, 1495 (1997).
[7] L. D. Muhlestein and G. C. Danielson, Phys. Rev. **158**, 825 (1967).
[8] H. R. Shanks, Solid State Commun. **15**, 753 (1974).
[9] L. F. Schneemeyer, F. J. DiSalvo, S. E. Spengler, and J. V. Waszczak, Phys. Rev. B **30**, 4297 (1984).
[10] P. B. Jamieson, S. C. Abrahams, and J. L. Bernstein, J. Chem. Phys. **48**, 5048 (1968).
[11] P. B. Jamieson, S. C. Abrahams, and J. L. Bernstein, J. Chem. Phys. **50**, 4352 (1969).
[12] M. H. Francombe and B. Lewis, Acta Crystallogr. **11**, 696 (1958).
[13] E. C. Subbarao, G. Shirane, and F. Jona, Acta Crystallogr. **13**, 226 (1960).
[14] J. Schneck and F. Denoyer, Phys. Rev. B **23**, 383 (1981).
[15] J. Schneck, J. C. Toledano, R. Whatmore, and F. W. Ainger, Ferroelectrics **36**, 327 (1981).
[16] C. Manolikas, G. Van Tendeloo, and S. Amelinckx, Solid State Commun. **58**, 845 (1986).
[17] T. Woike, V. Petříček, M. Dušek, N. K. Hansen, P. Fertey, C. Lecomte, A. Arakcheeva, G. Chapuis, M. Imlau, and R. Pankrath, Acta Crystallogr. Sect. B **59**, 28 (2003).
[18] H. A. Graetsch, C. S. Pandey, J. Schreuer, M. Burianek, and M. Mühlberg, Acta Crystallogr. Sect. B **70**, 743 (2014).
[19] L. A. Bursil and P. J. Lin, Philos. Mag. B **54**, 157 (1986).

[20] J. Schefer, D. Schaniel, V. Petříček, T. Woike, A. Cousson, and M. Wöhlecke, Z. Krist. **223**, 399 (2008).
[21] H. A. Graetsch, C. S. Pandey, J. Schreuer, M. Burianek, and M. Mühlberg, Acta Crystallogr. Sect. B **68**, 101 (2012).
[22] T. Kolodiazhnyi, H. Sakurai, O. Vasylkiv, H. Borodianska, and Y. Mozharivskyj, Appl. Phys. Lett. **104**, 111903 (2014).
[23] Although MgO has a high melting point, our previous studies of the BaO-MgO-Nb_2O_5 and BaO-MgO-Ta_2O_5 phase diagrams indicated that the small concentration of Mg can enter the TTB lattice and reduce the melting point of the TTB compounds, such as $Ba_9MgNb_{14}O_{45}$ and $Ba_9MgTa_{14}O_{45}$.
[24] Bruker SMART-NT Ver. 5.625, SAINT-PLUS Ver. 6.35A, SHELXTL Ver. 6.10; Bruker AXS Inc.: Madison, USA, 2002.
[25] See Supplemental Material at http://link.aps.org/supplemental/10.1103/PhysRevB.92.214508 for the anisotropic displacement parameters.
[26] Further information on the crystal structures can be found in the Supplemental Material and may be obtained from the Fachinformationszentrum Karlsruhe, 76344 Eggenstein-Leopoldshafen, Germany [fax: (49) 7247-808-666; email: crysdata@fiz.karlsruhe.de], by quoting the CSD depository numbers 430177 for $Ba_6Nb_{10}O_{30}$and 430178 for $Sr_6Nb_{10}O_{30}$.
[27] E. Lee, C.-H. Park, D. P. Shoemaker, M. Avdeev, and Y.-I. Kim, J. Solid State Chem. **191**, 232 (2012).
[28] T. Kolodiazhnyi, H. Sakurai, O. Vasylkiv, H. Borodianska, S. Forbes, and Y. Mozharivskyj, Appl. Phys. Lett. **105**, 062902 (2014).
[29] R. Berman, *Thermal Conduction in Solids* (Clarendon, Oxford, 1976).
[30] Over the course of this study it was found that the small humps in the thermal conductivity of the $Ba_{6-x}Sr_xNb_{10}O_{30}$samples at $T = 160$–190 K reported in Ref. [22] are instrumental artifacts.
[31] P. M. Chaikin, *in Organic Superconductivity*, edited by V. Z. Kresin, W. A. Little (Plenum Press, New York, 1990), pp. 101–114.
[32] A. K. Geim, S. V. Dubonos, J. G. S. Lok, M. Henini, and J. C. Maan, Nature (London) **396**, 144 (1998).
[33] K. Takada, H. Sakurai, E. Takayama-Muromachi, F. Izumi, R. A. Dilanian, and T. Sasaki, Nature (London) **422**, 53 (2003).
[34] M. Sigrist and K. Ueda, Rev. Mod. Phys. **63**, 239 (1991).
[35] N. Haldolaarachchige, Q. Gibson, J. Krizan, and R. J. Cava, Phys. Rev. B **89**, 104520 (2014).
[36] E. Fischer, W. Hässler, and E. Hegenbarth, Phys. Status Solidi A **72**, K169 (1982).
[37] M. Tachibana and E. Takayama-Muromachi, Phys. Rev. B **79**, 100104(R) (2009).
[38] W. A. Phillips, Rep. Prog. Phys. **50**, 1657 (1987).
[39] C. L. Choy, W. P. Leung, T. G. Xi, Y. Fei, and C. F. Shao, J. Appl. Phys. **71**, 170 (1992).
[40] M. Tachibana, T. Kolodiazhnyi, and E. Takayama-Muromachi, Appl. Phys. Lett. **93**, 092902 (2008).
[41] J. B. Goodenough, Prog. Solid State Chem. **5**, 145 (1971).
[42] N. E. Brese and M. O. O'Keeffe, Acta Crystallogr. Sect. B **47**, 192 (1991).
[43] N. F. Mott, *Metal-Insulator Transitions* (Taylor & Francis, London, 1974).
[44] K. Isawa, J. Sugiyama, K. Matsuura, A. Nozaki, and H. Yamauchi, Phys. Rev. B **47**, 2849 (1993).
[45] T. Wolfram, Ş. Ellialtioğlu, *Electronic and optical properties of d-band perovskites* (Cambridge University Press, Cambridge, 2006).
[46] S. Ya. Istomin, G. Svensson, O. G. D'yachenko, W. Holm, and E. V. Antipov, J. Solid State Chem. **141**, 514 (1998).
[47] P. W. Anderson, Phys. Rev. **109**, 1492 (1958).
[48] P. P. Edwards and M. J. Sienko, Phys. Rev. B **17**, 2575 (1978).